Hyperspectral image processing and analysis

B. Krishna Mohan* and Alok Porwal

Centre of Studies in Resources Engineering, Indian Institute of Technology (Bombay), Mumbai 400 076, India

Hyperspectral data pose challenges to image interpretation, because of the need for calibration, redundancy in information, and high data volume due to large dimensionality of the feature space. In this article, a general framework is presented for working with hyperspectral imagery, including removal of atmospheric effects, imaging spectroscopy, dimensionality reduction and classification of imagery. The phenomenon of mixture modelling is briefly discussed, followed by a recent development in mapping the classes at sub-pixel level based on the principle of super-resolution.

Keywords: Atmospheric correction, classification, feature selection, hyperspectral image.

Introduction

MULTISPECTRAL image analysis methods largely depend on the spatial aspects of the objects of interest such as their shape, texture and spectral properties in the few wavelength bands in which the images are acquired. It is difficult with such data to discriminate between vegetation categories, eutrophication of lakes, identify presence or absence of specific elements or compounds in a soil or rock, and so on. For this purpose, a highly detailed spectral characterization of the target is required and the field of hyperspectral remote sensing has evolved to address this need.

Compared to conventional remote sensing, hyperspectral sensors acquire data in narrow wavelength bands of width of the order of 10 nm. The 'hyper' in hyperspectral refers to the large number of wavelength bands, and the distinguishing factor for hyperspectral sensors is that the applicable wavelength range is covered by detector elements operating in narrow and contiguous wavelength bands. Hyperspectral images are spectrally over-determined (that is, there is high correlation between adjacent bands), and they provide adequate spectral detail to identify and distinguish between spatially similar-looking objects having moderate spectral differences. A simple and easy introduction to this subject is provided by Shippert[1]. One of the popular hypserspectral sensors is the airborne visual infrared imaging spectrometer (AVIRIS) on aircraft platform. Among spaceborne systems, NASA's EOS-1 satellite platform with Hyperion sensor having

10 nm bandwidth in each wavelength band and covering a range of 400–2500 nm provided extremely useful data.

Framework for hyperspectral image analysis

A generic framework for hyperspectral image analysis (Figure 1) comprises mandatory initial image corrections followed by two different approaches for extracting information from the images.

The first one is based on the imaging spectroscopy approach wherein the presence of specific target materials in the image is detected by matching the corrected pixel spectra with reference spectra from a spectral library. Techniques like spectral angle mapper are used for matching the pixel spectra with the reference spectra. Further, the reference spectra can also be used to define target classes of interest and determine the relative proportion of pure classes within mixed pixels. Mixed pixels are characterized by being different from all known spectra in the spectral library and being comparable in distance to more than one reference spectrum.

The image analysis approach to working with hyperspectral images starts with correcting the image for atmospheric distortions. At this point there will be a major departure from the imaging spectroscopy approach, and the dimensionality of the hyperspectral image is reduced to cope with the computational cost as well as demands on ground truth for supervized classification purposes. The reduced dimensionality data are subjected to image classification based on standard machine learning algorithms like support vector machine (SVM) and neural network[2]. A second approach that is similar to the imaging spectroscopy approach is the extraction of reference spectra from the image itself corresponding to different target classes and then identifying the mixture proportions of different target classes within the pixels in the image. While the mixture models provide estimates of the relative areas of the classes within a mixed pixel, the actual layout of such classes within a pixel is not available. Sub-pixel classification is an emerging area in hyperspectral image analysis to address this issue and this is discussed in detail in a later section.

Atmospheric corrections

The approaches to atmospheric corrections of hyperspectral data range from simple image-based empirical line

---

*For correspondence. (e-mail: bkmohan@csre.iitb.ac.in)

and flat-field techniques to more advance radiative transfer modelling techniques. Some of the main algorithms are discussed in the following sections, and are drawn from various sources[3].

Empirical atmospheric correction approaches

Several image-based empirical approaches to atmospheric corrections have been developed for deriving relative surface reflectance of ground pixels. The most widely used techniques for atmospheric correction of land surface images include the flat-field correction[4], the internal average reflectance approach[5] and the empirical line approach[6]. Although an absolute radiometric calibration of hyperspectral imagers is not required when using the empirical approaches for the estimation of relative surface reflectance, the hyperspectral imaging system must remain stable over the duration of data acquisition.

The flat-field correction approach is based on the assumption that the image contains an area that is comprised exclusively of spectrally featureless material, i.e. it has similar reflectance in all wavelengths. The spectral features in the composite spectrum of such an area are considered to be entirely due to atmospheric gases and aerosols. Further, assuming a homogenous atmosphere over the entire image area, this composite spectrum is used to normalize the spectral reflectance curves of all pixels in the image.

The internal average reflectance approach involves calculating the average spectrum of the entire image. The spectra of all pixels in the image are then normalized by dividing with the average reflectance spectrum. This approach is generally used in arid areas devoid of significant vegetation cover.

The above approaches do not require field measurements of spectral reflectance of ground material and derive all input parameters from the image itself. However, the output relative reflectance spectra often have artefacts that are not present in the laboratory or field reflectance spectra of comparable materials[3,7]. This could be because of the fact that the flat-field spectra may contain some absorption features due to surface materials in addition to those due to atmospheric absorption features, since it is difficult to find a naturally occurring material that is spectrally 100% flat. As pointed out[3], the use of such spectrum in the derivation of relative reflectance spectra of other pixels can introduce broad absorption bands in the resulting spectra.

The empirical line approach requires field measurements of reflectance spectra for at least one bright target and one dark target. The hyperspectral data over the surface targets are linearly regressed against the field reflectance spectra to derive the linear equation relating hyperspectral data to the ground reflectance. The linear equation is then applied to the whole image for the derivation of surface reflectance for the entire scene. This method produces spectra that are comparable to reflectance spectra measured in the field or in the laboratory[8]. However, if changes occur in the atmospheric properties outside the area used for the empirical line approach, which is often the case, the spectral reflectance data will contain atmospheric features[3].

Radiative transfer modelling approaches

The radiative transfer modelling approaches are based on explicit simulation of the absorption and scattering effects of atmospheric gases and aerosols. However, the molecular absorptions due to a majority of the thirty-odd gases present in the Earth's atmosphere in the visible-near infrared–short-wave infrared region (VNIR–SWIR; 0.4 to 2.5 μm) is negligible at the typical spectral resolutions of the hyperspectral sensors (1–20 nm[3]). Only eight gases, namely, water vapour (H_2O), carbon dioxide (CO_2), ozone (O_3), nitrous oxide (N_2O), carbon monoxide (CO), methane (CH_4), oxygen (O_2) and nitrogen dioxide (NO_2) produce observable absorption features (Figure 2).

In Figure 2, the short wavelength region between 0.4 and 0.7 μm is strongly affected by molecular scattering (Rayleigh scattering). The Rayleigh scattering decreases rapidly with increasing wavelength at the rate of λ^{-4}. The aerosol scattering also decreases with increasing wavelength, but at a slower rate of λ^{-2} to λ^{-1}.

Hyperspectral data are generally distributed in the form of radiometrically corrected datasets containing registered radiance at the spaceborne or airborne hyperspectral sensor. At-the-sensor radiance is composed of two components: (i) upwelling atmospheric path radiance (due to Rayleigh and aerosol scattering), and (ii) transmitted components of the surface-reflected solar radiances that were not absorbed by the atmospheric gases and
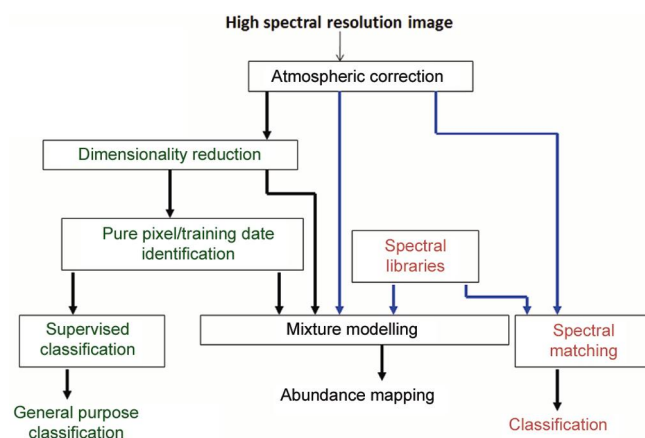

Figure 1. Framework for hyperspectral image analysis.

aerosols. These radiances are often converted to apparent reflectance[9,10]. The apparent reflectance is given by

$$\rho_{\text{obs}}^*(\lambda, \theta, \varphi, \theta_0, \varphi_0) = \frac{\pi L_{\text{obs}}(\lambda, \theta, \varphi, \theta_0, \varphi_0)}{\mu_0 F_0(\lambda)}, \quad (1)$$

where θ_0 is the solar zenith angle, φ_0 the solar azimuth angle, θ the sensor zenith angle, φ the sensor azimuth angle, λ the wavelength, L_{obs} the radiance measured at the satellite, F_0 the solar flux at the top of the atmosphere when the solar zenith angle is equal to zero, and μ_0 is the cosine of solar zenith angle. Apparent reflectance is a measure of the reflectivity for the atmosphere and surface system. When the surface is assumed to be Lambertian and the adjacency effect is neglected[10], $\rho_{\text{obs}}(\lambda, \theta, \varphi, \theta_0, \varphi_0)$ can be expressed approximately[3]

$$\rho_{\text{obs}}^*(\lambda, \theta, \varphi, \theta_0, \varphi_0) = \left\{ \rho_{\text{atm}}^*(\lambda, \theta, \theta_0, \varphi_0) \right.$$
$$\left. + \frac{t_d(\lambda, \theta_0)t_u(\lambda, \theta)\rho(\lambda)}{1 - s(\lambda)\rho(\lambda)} \right\} T_g(\lambda, \theta, \theta_0), \quad (2)$$

where ρ_{atm} is the path reflectance, t_d the downward scattering transmittance, t_u the upward scattering transmittance, s the spherical albedo of the atmosphere, ρ the surface reflectance, and T_g the total gaseous transmittance in the Sun-surface-sensor path. The first term in the bracket, ρ_{atm}, is the contribution from atmospheric
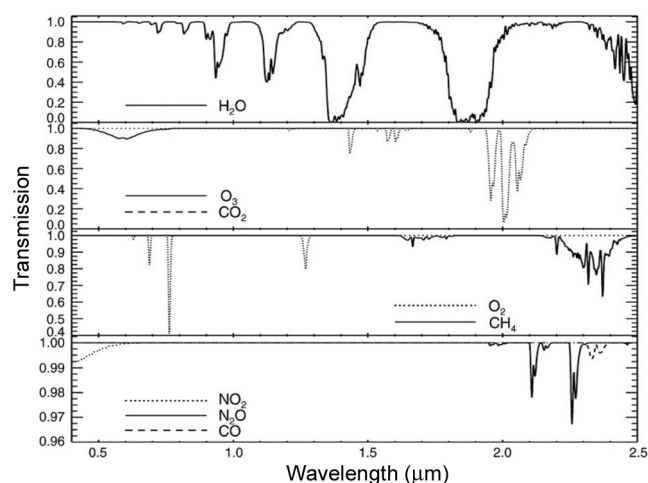

Figure 2. Simulated transmittance spectra of atmospheric water vapour, carbon dioxide, ozone, nitrous oxide, carbon monoxide, methane, oxygen and nitrogen dioxide. The path is specified for a solar zenith angle of 50°, nadir-viewing, a sea-level surface and a sensor at the top of the atmosphere. Typical amounts of each gas are used. The legends of each plot indicate the gas in each one. The horizontal scales of each plot are identical; the vertical scales are different. The spectra are simulated at a sampling interval of 1 nm and with a spectral resolution of 5 nm (source: Gao *et al.*[3]).

scattering to the measured apparent reflectance (the noise part). The second term in the bracket ($t_d t_u \rho/(1 - s\rho)$) is the radiance reflected by the ground pixel (the signal). The term t_s contains absorption bands of all atmospheric gases (Figure 1). The atmospheric scattering and gaseous absorption are treated as two independent processes. The coupling effects between the two are neglected. In the real atmosphere, the scattering and absorption processes occur simultaneously. The coupling effects are small in regions where the atmospheric gaseous absorptions are weak and also in regions where the scattering effects are small.

Solving eq. (2) for the reflectance ρ of the ground pixel and simplifying the notations for relevant quantities yields[3]

$$\rho = \frac{\rho_{\text{obs}}^*/(T_g - \rho_{\text{atm}}^*)}{t_d t_u + s\{\rho_{\text{obs}}^*/(T_g - \rho_{\text{atm}}^*)\}}. \quad (3)$$

By simulating the atmospheric quantities T_g, ρ_{atm}, t_d, t_u, and s with radiative transfer models, the reflectance for a Lambertian ground pixel (ρ) can be retrieved from the measured radiance, L_{obs}, using the above eqs (1)–(3). The simulations are performed using computer codes that model the atmospheric propagation of electromagnetic radiations at different wavelengths. The most widely used code is MODTRAN (MODerate resolution atmospheric TRANsmission) developed by Spectral Sciences Inc. and the US Air Force. This code models the atmospheric propagation of electromagnetic radiations in the 100–50,000 cm^{-1} (0.2–100 μm) spectral range[11]. Another popular code is 6S (second simulation of a satellite signal in the solar spectrum), an advanced radiative transfer code designed to simulate the reflection of solar radiation by a coupled atmosphere–surface system for a wide range of atmospheric, spectral and geometrical conditions[12]. DISORT (Discrete Ordinates Radiative Transfer programme for a multi-layered plane-parallel medium) is a general and versatile plane-parallel radiative transfer programme for modelling the propagation of the electromagnetic radiation in the ultraviolet to the radar regions[13]. A large number of commercial atmospheric correction algorithms such as ATREM, HATCH, ACORN, FLAASH, ISAD, etc. have now been developed and integrated with popular commercial satellite image processing software such as ENVI, ERDAS, PCI Geomatica, etc.

Most of the commercial atmospheric correction algorithms use the above radiative transfer codes for simulating the atmospheric parameters. However, they use different techniques for estimating the input parameters for simulation. As mentioned above, only six gases cause significant absorption in the VNIR–SWIR regions. Among them, only water vapour concentration can have significant spatial variation from pixel to pixel. These algorithms generally use channel ratio technique[9] for estimating the water vapour column over every pixel. The water vapour

transmittance spectrum in the VNIR–SWIR region is then simulated using a radiative transfer code. The transmission spectra of carbon dioxide, ozone, nitrous oxide, carbon monoxide, methane and oxygen in the VNIR–SWIR region are simulated based only on the solar and observational geometry because their concentrations do not vary significantly at the pixel-scale. The scattering effect due to atmospheric molecules and aerosols is modelled using radiative transfer codes. The input aerosol concentrations are estimated based on the user-selected standard aerosol model and visibility range. The output of commercial atmospheric correction algorithms is the ground reflectance data cube.

Imaging spectroscopy

Hyperspectral remote sensing or imaging spectroscopy involves acquiring images in a large number of narrow contiguous spectral bands (typically >100). Consequently, hyperspectral images are better described as image cubes with two spatial dimensions and the third spectral dimension. It is used in a variety of domains, including planetary and terrestrial geology, agriculture, forestry, coastal and inland water studies, atmospheric studies, environment hazards assessment and urban studies.

Because of the quantization of various types of nuclear, electronic and molecular energy levels, different materials absorb energy of specific wavelengths and, as a result, reflectance varies with wavelength. Reflectance imaging spectroscopy involves measuring spectral reflectance, that is, the ratio of reflected energy to incident energy as a function of wavelength. The plots of spectral reflectance are called spectral reflectance curves or reflectance spectra. Each material has a unique chemical composition and physical structure, and therefore unique nuclear, electronic and molecular energy levels; as a result each material has a unique spectral reflectance curve (Figures 3 and 4).

The spectra in Figures 3 and 4 show distinct absorption features at different wavelengths. The vegetation spectrum (Figure 3) shows strong absorption in the visible region, but has relatively lower absorption of green wavelength compared to red and blue wavelength. The absorption in the near infrared region is very low, except small absorption features at 0.9, 1.2 and 1.4 μm, which is because of molecular vibrations of H_2O. The mineral spectra too show distinct features. Hydroxyl-bearing minerals (kaolinite and montmorillonite) show hydroxyl absorption features at 1.4, 1.9 and 2.1–2.2 μm. Hematite shows a broad Fe absorption feature around 0.9 μm, while calcite shows features related to CO_2 absorption in 1.9–2.4 μm region. Orthoclase has a flat spectrum in the entire region, implying that it is not possible to identify this mineral in the visible – shortwave infrared region. This mineral shows spectral features in the thermal infrared region.

Materials are identified from hyperspectral remote sensing images by comparing their spectra to a set of reference spectra. Several libraries of reflectance spectra of natural and man-made materials are available for public use. The ASTER spectral library has been made available by NASA as part of the advanced spaceborne thermal emission and reflection radiometer (ASTER) imaging instrument programme. It includes spectral compilations from NASA's Jet Propulsion Laboratory, Johns Hopkins University, and the United States Geological Survey. The ASTER spectral library currently contains nearly 2000 spectra, including minerals, rocks, soils, man-made materials, water and snow, covering the entire wavelength region from 0.4 to 14 μm (ref. 14). The library is accessible interactively via the worldwide web at http://speclib.jpl.nasa.gov. Most of the commercial image processing software have built-in spectral libraries.

Several spectral matching techniques are available for obtaining surface compositional information on a pixel-by-pixel basis from hyperspectral images[15]. Techniques that specifically use absorption band position and depth include the relative absorption band-depth (RBD) approach[16], the spectral feature fitting (SFF) technique[17], the TRICORDER[18] and TETRACORDER[19] algorithms
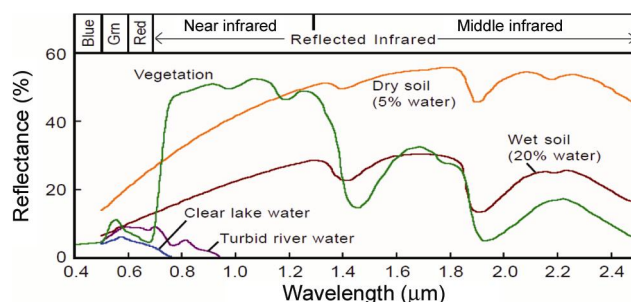

Figure 3. Reflectance spectra for several common Earth surface materials over the visible light to reflected infrared spectral range[14].
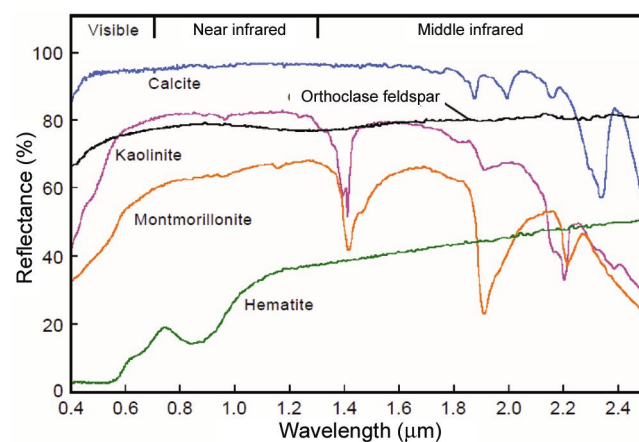

Figure 4. Reflectance spectra for important minerals over the visible light to reflected infrared spectral range[14].

developed at the USGS spectral laboratory and spectral angle mapper (SAM) algorithm[20]. These techniques work on continuum-removed reflectance spectra, based on the assumption that reflectance spectra have two components: a continuum or the broad shape of the spectra and individual absorption features (Figure 5).

The RBD images provide a local continuum correction removing any small channel-to-channel radiometric offsets, as well as variable atmospheric absorption and solar irradiance drop-off for each pixel in the dataset. To produce a RBD image, several data channels from both absorption band shoulders are summed and then divided by the sum of several channels from the absorption band minimum. The resulting absorption band-depth image gives the depth of an absorption feature relative to the local continuum, which can be used to identify pixels having stronger absorption bands, indicating that these may represent a certain mineral.

The SFF technique uses continuum removed pixel spectra, which are compared to continuum reference spectra of known mineralogy. A least-squares fit is calculated band-by-band between each reference end-member and the unknown (continuum removed) pixel spectra. A 'scale' image is produced for each end-member selected for analysis by first subtracting the continuum-removed spectra from one, thus inverting them and making the continuum zero. A large scale-factor is equivalent to a deep spectral feature, while a small scaling factor indicates a weak spectral feature. A least-squares-fit is then calculated band-by-band between each reference end-member and the unknown spectrum. The total root-mean-square (RMS) error is used to form an RMS error image for each end-member. The ratio of the scale image and the RMS image provides a 'fit' image that is a measure of how well the unknown spectrum matches the reference spectrum on a pixel-by-pixel basis.

The Tricorder and its successor Tetracorder use a two-step algorithm. First, the local spectral slope (the 'continuum') is estimated and removed both from
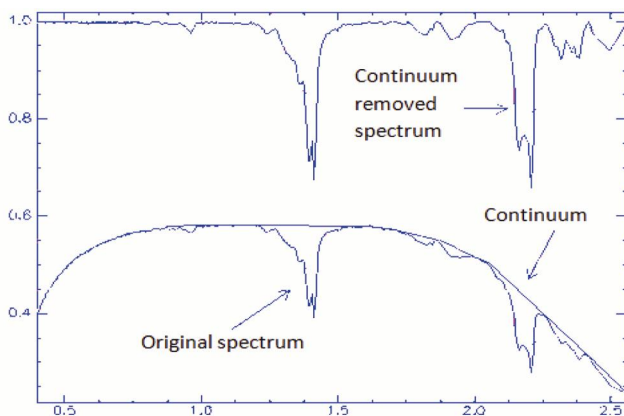
reference and observed spectra. Next, the identification of materials from their spectra is constrained by: (a) the goodness of fit of a spectral feature to a reference, (b) reflectance level, (c) continuum slope and (d) presence or absence of key ancillary spectral features. The Tetracorder uses these reference continuum-removed spectral features to compute a weighted fit between unknown spectra and known library spectra. The surface compositional information is derived and results are validated using an expert system approach.

The SAM technique involves the calculation of spectral similarity between the pixel spectrum and a reflectance spectrum assuming that the data are correctly calibrated to apparent reflectance with dark current and atmospheric effects have been removed (see next section). The spectral similarity between the pixel spectrum, t, and the reference (or laboratory) spectrum, r, is expressed in terms of the average angle between the two spectra in an n-dimensional spectral space as follows

$$\theta = \cos^{-1}\left[\frac{\sum\limits_{i=1}^{n} t_i r_i}{\sum\limits_{i=1}^{n} t^2 \sum\limits_{i=1}^{n} r^2}\right]. \tag{4}$$

In this approach, the spectra are treated as vectors in a spectral feature space with dimensionality equal to the number of bands, n. The outcome of the spectra angle mapping for each pixel is an angular difference measured in radians ranging from zero to $\pi/2$, which gives a qualitative estimate of the presence of absorption features which can be related to composition.

However, the fundamental requirement for successful implementation of spectral matching algorithm is the retrieval of ground pixel reflectance from the at-the-sensor radiance. The procedure used to estimate spectral reflectance from at-the-sensor radiance is called 'atmospheric correction' and involves accurate estimation and compensation of the scattering and absorption due to atmospheric gases.

Dimensionality reduction

In some applications such as land-use/land-cover mapping, the objective is supervized or unsupervized classification of the hyperspectral image; in such cases it is not necessary that the classification is implemented in the spectral space. As a matter of fact, it is preferable to implement image classification in a low-dimensional feature space in order to minimize the problem of limited ground truth. Statistical techniques such as principal components rotation, minimum noise fraction transformation or independent components rotation can be used for this purpose. However, in other applications such as

Figure 5. Continuum removal from reflectance spectrum.

geological mapping, soil characterization, agriculture crop monitoring, etc. the retrieval of surface properties is the main objective. In such cases the processing and analyses has to be carried out in the spectral space only and is entirely based on pixel reflectance spectra.

The minimum noise fraction (MNF) transformation is used to reduce the dimensionality of the hyperspectral data by segregating the noise in the data. The MNF transform is a linear transformation which is essentially two cascaded principal components analysis (PCA) transformations. The first transformation, based on an estimated noise covariance matrix decorrelates and rescales the noise in the data. This results in transformed data in which the noise has unit variance and no band-to-band correlations. The second transformation is a standard PCA of the noise-whitened data[21]. MNF transformation computes the normalized linear combinations of the original bands which maximize the ratio of the signal to noise. The approach was developed specifically for analysis of multiple band remotely sensed data which would produce orthogonal bands ordered by their information content. It can also be used for reducing noise through application of filters matched to the noise characteristics of the transformed bands and inverting the data.

As the transform is based on a signal-to-noise ratio, it is also invariant with respect to scale changes in bands. Additionally, the signal and noise of the transformed bands are also orthogonal. The approach requires that the covariance of the noise be known, which is not generally the case for remotely sensed data. A reasonable estimate of the noise in each band can be obtained when the signal is highly correlated across bands through adaptation of a procedure called the maximum autocorrelation factor, which exploits the correlation of signals in spatial neighbourhoods[22]. Among other transform-based techniques, the independent component analysis (ICA) is popularly used in analysing hyperspectral images and a good source for the same will be Varshney and Arora[23].

An alternative to reducing dimensionality by transforming the input image dataset to a new feature space is to choose a subset of the original bands such that they retain enough capability to separate the data into distinct classes with least amount of error or with the highest amount of accuracy possible. Due to high dimensionality of the original data space, brute force choosing a subset (for example selecting, 25 from 160 bands) involves evaluating too many combinations and therefore efficient search techniques are required. Genetic algorithms (GAs) are good choice due to the fact that they can utilize all the domain knowledge while coming up with an optimum solution.

Simple genetic algorithms are quite well known even in remote sensing applications and hence they are not elaborated here. Interested readers can consult Goldberg[24] for a basic introduction to the subject. Genetic algorithms have been the preprocessor to generate initial weights for a multilayer perceptron neural network[25].

In this article, a modified version of the conventional genetic algorithm, known as the multipopulation genetic algorithm (MGA) is presented (Figure 6) that has promise to overcome the problem of premature convergence occurring in simple GAs and can produce better results in a short execution time. Previous research has shown that MGAs have been used in a variety of problems, including feature selection, but a very little is known of them being used for dimensionality reduction for the hyperspectral images[26].

MGA parameters that control the migration process are summarized as: (i) Topology – two parallel evolving subpopulations; (ii) Migration policy – best–worst exchange; (iii) Migration rate – half of the candidates migrate and (iv) Migration interval – 10 generations.

The above parameters were chosen as the best combination after several runs of the experiment. The results of MGA approach to dimensionality reduction were compared with the results of ICA, MNF and simple genetic algorithm approaches and it was found that, in general, MGA was producing results that were as good as or better than a best of the results produced by the other methods. The overall workflow is given in Figure 7 for analysing the hyperspectral images through atmospheric correction, dimensionality reduction and comparison of results.

The best performance with genetic algorithms was observed with the MGA topology. It was found that the classification error with the test samples was least as a function of genetic iteration for MGA compared to simple GA (SGA) topology. In Figure 8, the y-axis indicates the classification error, and hence best fitness value corresponds to the least error. As is evident from the well-known Hughes phenomenon, the classification error generally increases with the dimensionality beyond a point, if it is not matched by a corresponding increase in the number of training data, in Tables 1 and 2, the classification accuracies computed for full 155 bands dataset and a reduced (30 bands) dataset illustrate the same trend.
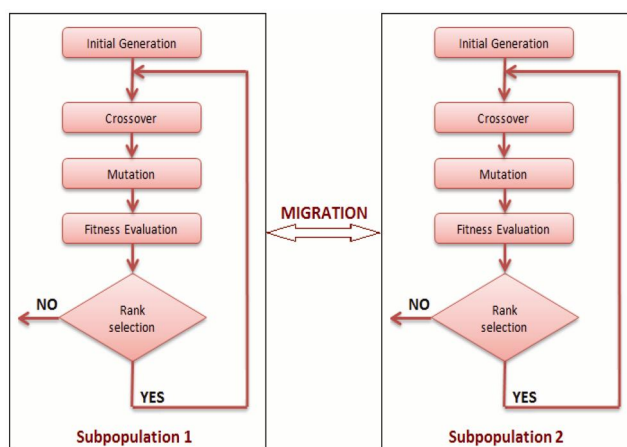

Figure 6. Flowchart for the multipopulation genetic algorithm (MGA) used in this study.

Table 1. Confusion matrix for classified image using all 155 bands for imageSubset1

Class	Vegetation	Water	Built-up areas	Open land	Total
Vegetation	2055	0	6	3	2064
Water	0	563	0	0	563
Built-up	1	0	1072	4	1077
Open land	112	1	269	1330	1712
Total	2168	564	1347	1337	5416
	Overall accuracy = 92.6883%		Kappa coefficient = 0.8969		

Table 2. Confusion matrix for classified image using MGA selected 30 bands for imageSubset1

Class	Vegetation	Water	Built-up areas	Open land	Total
Vegetation	2107	0	0	8	2115
Water	0	552	1	1	554
Built-up	0	2	1165	23	1190
Open land	61	10	181	1305	1557
Total	2168	564	1347	1337	5416
	Overall accuracy = 94.7009%		Kappa coefficient = 0.9251		
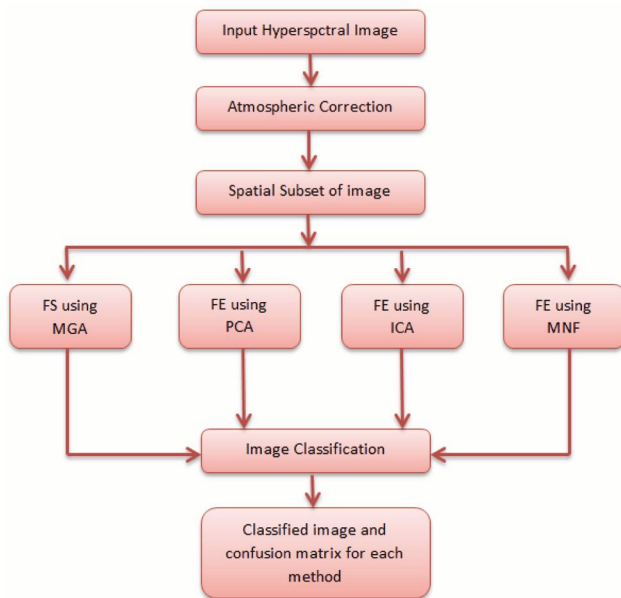
Figure 7. Workflow of the MGA methodology.

Figure 8. Classification error versus genetic iterations (generations). Note that the plots actually denote classification error and hence best fitness value corresponds to least classification error.

Classification

Two hyperspectral subset images from Mumbai 2008 Hyperion image were classified and the results for full 155 bands and 30-band reduced set are shown in Tables 3 and 4. The results indicate the advantage of reducing a highly correlated dataset to a reduced dataset. The nearest neighbour classifier was used due to its simplicity and its similarity to the spectral angle mapper in spirit. It is evident that the reduced dataset has performed better than the full 155-band dataset because any noise in some of the bands would be eliminated in the reduced set. The kappa coefficient and class-wise accuracy are also shown for two images.
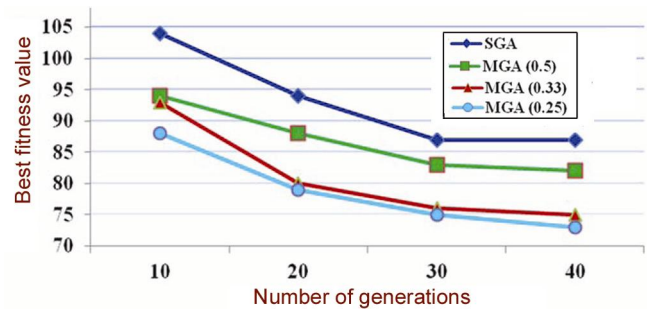
Super-resolution

The above classification process treated each pixel as belonging to a single class, while in hyperspectral remote sensing, due to coarse spatial resolution, it is inevitable that majority of the pixels would be a mixture of more than one class. While standard mixture models allow us to estimate the relative proportions of different classes within a pixel, the spatial arrangement of the classes within the pixel is not known. Sub-pixel classification is still evolving, and in principle these approaches attempt to analyse the pixels at a higher resolution than what was acquired at. These approaches are also termed super-resolution techniques for this reason.

Hopfield neural networks are known in neural network literature for their ability to be used as content-addressable memory, wherein the access is not by address of the memory cell but by part of the content stored in that cell. It is also used in image restoration where the distortion-free image is estimated from its degraded version. Hopfield neural networks were employed in super-resolution
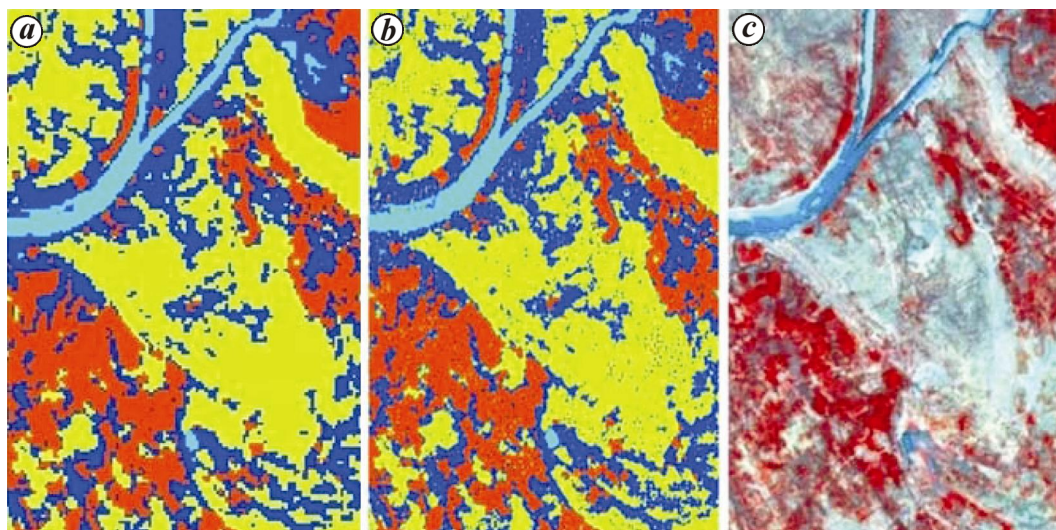
Figure 9. Example of super-resolution: *a*, Classification of original 30 m resolution Hyperion image. *b*, Classification output by super-resolution to 10 m resolution. *c*, Pan-sharpened Landsat 8 image at 10 m resolution for reference (all processing performed on the Hyperion image only).

Table 3. Accuracy and kappa coefficient for all datasets used for classification for imageSubset1

Dataset used for classification	Overall accuracy (%)	Kappa coefficient
Classification with all 155 bands	92.6883	0.8969
MGA reduced 30 bands	94.7009	0.9251
PCA transformed 30 components	94.1654	0.9176
MNF transformed 30 components	93.8146	0.9127
ICA transformed 30 components	94.6455	0.9244

Table 4. Accuracy and kappa coefficient for all datasets used for classification for imageSubset2

Dataset used for classification	Overall accuracy (%)	Kappa coefficient
Classification with all 155 bands	93.4378	0.9104
MGA reduced 30 bands	96.0134	0.9442
PCA transformed 30 components	94.7816	0.9271
MNF transformed 30 components	94.7144	0.9262
ICA transformed 30 components	94.7816	0.9271

estimation of sub-pixel layout of the classes in hyperspectral remote sensing based on the coarse resolution pixel as input[27]. The approach here is to use classes assigned to adjacent pixels and use continuity from the current pixel to the neighbouring pixel as a constraint[28].

A simple approach to super-resolution is reported here wherein the mixture proportions of different classes are approximated by the fuzzy C-mean algorithm given memberships at each pixel into different classes. Using these membership as well as the continuity with neighbouring pixels condition[29], the sub-pixel classes are estimated. The results are provided in Figure 9 which show the zoomed version of the full pixel classification and the corresponding sub-pixel classification. The results are promising and it is planned to combine the sub-pixel classification with proper linear mixture model with non-negativity and unit-sum abundance proportion conditions.

Summary

In this article an introduction is given to hyperspectral image analysis, including issues of atmospheric corrections and imaging spectrometry. Under image analysis, a new approach to dimensionality reduction based on MGA is described and a brief description of super-resolution based on an adaptation of Hopfield neural network is provided. The field of hyperspectral remote sensing and image analysis is expanding quite rapidly and more developments in terms of spatial resolution and spectral resolution using sensors mounted on aircraft and unmanned aerial vehicles will be a reality in near future.

1. Shippert, P., Introduction to hyperspectral image analysis, 2008; http://satjournal.tcom.ohiou.edu/pdf/shippert.pdf (accessed on May 2008).
2. Haykin, S., *Neural Networks and Learning Machines*, Prentice-Hall, 2008.
3. Gao, B., Montes, M. J., Davis, C. O. and Goetz, A. F. H., Atmospheric correction algorithms for hyperspectral remote sensing data of land and ocean. *Remote Sensing Environ.*, 2009, **113**, 17–24.
4. Roberts, D. A., Gardner, M., Church, R., Ustin, S., Scheer, G. and Green, R. O., Mapping Chaparral in the Santa Monica Mountains using endmember spectral mixture models. *Remote Sensing Environ.*, 1998, **65**, 267–279.
5. Kruse, F. A., Use of airborne imaging spectrometer data to map minerals associated with hydrothermally altered rocks in the

northern Grapevine Mountains, Nevada and California. *Remote Sensing Environ.*, 1988, **24**, 31–51.

6. Conel, J. E., Green, R. O., Vane, G., Bruegge, C. J. and Alley, R. E., AIS-2 radiometry and a comparison of methods for the recovery of ground reflectance, In Proceedings of the Third Airborne Imaging Spectrometer Data Analysis Workshop, Jet Propulsion Laboratory, Pasadena, CA, JPL, 87–30, 1987, pp. 18–47.

7. Clark, R. N. and King, T. V. V., Causes of spurious features in spectral reflectance data. In Proceedings of the Third Airborne Imaging Spectrometer Data Analysis Workshop, JPL, 1988, vol. 87–30, pp. 49−61.

8. Aspinall, R. J., Marcus, W. A. and Boardman, J. W., Considerations in collecting, processing, and analyzing high spatial resolution hyperspectral data for environmental investigations. *J. Geogr. Syst.*, 2002, **4**, 15–29.

9. Gao, B., Heidebrecht, K. B. and Goetz, A. F. H., Derivation of scaled surface reflectances from AVIRIS data. *Remote Sensing Environ.*, 1993, **44**, 165–178.

10. Tanre, D., Deroo, C., Duhaut, P., Herman, M., Morcrette, J. J., Perbos, J. and Deschamps, P. Y., *Simulation of the Satellite Signal in the Solar Spectrum (5S), User's Guide*, U.S.T. de Lille, 59655, Laboratoire d' Optique Atmospherique, Villeneuve d'ascq, France, 1986.

11. Berk, A., Bernstein, L. S., Anderson, G. P., Acharya, P. K., Robertson, D. C., Chetwynd, J. H. and Adler-Golden, S. M., MODTRAN cloud and multiple scattering upgrades with application to AVIRIS. *Remote Sensing Environ.*, 1998, **65**, 367–375.

12. Kotchenova, S. Y., Vermote, E. F., Matarrese, R. and Klemm, F. J., Validation of a vector version of the 6S radiative transfer code for atmospheric correction of satellite data. Part I: Path radiance. *Appl. Opt.*, 2006, **45**, 6762–6774.

13. Stamnes, K., Tsay, S. C., Wiscombe, W. and Jayaweera, K., Numerically stable algorithm for discrete-ordinate-method radiative transfer in multiple scattering and emitting layered media. *Appl. Opt.*, 1988, **27**, 2502–2509.

14. Smith, R. B., Remote sensing of environment – a tutorial, 2012; http://www.microimages.com/documentation/Tutorials/introrse.pdf (accessed on 30 September 2014).

15. Van Der Meer, F., De Jong, S. and Bakker, W., Imaging spectrometry: basic analytical techniques. In *Imaging Spectrometry: Basic Principles and Prospective Applications* (eds van der Meer, F. and de Jong, S.), Kluwer Academic Publishers, Dordrecht, The Netherlands, 2001, pp. 17–61.

16. Crowley, J. K., Brickey, D. W. and Rowan, L. C., Airborne imaging spectrometer data of the Ruby mountains, Montana: mineral discrimination using relative absorption band-depth images. *Remote Sensing Environ.*, 1989, **29**, 121–134.

17. Clark, R. N., Gallagher, A. J. and Swayze, G. A., Material absorption band depth mapping of imaging spectrometer data using the complete band shape least-squares algorithm simultaneously fit to multiple spectral features from multiple materials. In Proceedings of the Third Airborne Visible/Infrared Imaging Spectrometer (AVIRIS) Workshop, JPL, 1990, vol. 90–54, pp. 176–186.

18. Crowley, J. K. and Swayze, G. A., Mapping minerals, amorphous materials, environmental materials, vegetation, water, ice, and other materials: the USGS tricorder algorithm. In Summaries of the Fifth Annual JPL Airborne Earth Science Workshop, JPL, 1995, vol. 95-1, pp. 39–40.

19. Clark, R. N. *et al.*, Imaging spectroscopy: earth and planetary remote sensing with the USGS tetracorder and expert systems. *J. Geophys. Res.*, 2003, **108**, 1–44.

20. Kruse, F. A., Lefkoff, A. B., Boardman, J. B., Heidebrecht, K. B., Shapiro, A. T., Barloon, P. J. and Goetz, A. F. H., The spectral image processing system (SIPS) – interactive visualization and analysis of imaging spectrometer data. *Remote Sensing Environ.*, 1993, **44**, 145–163.

21. ENVI tutorial (http://www.cstars.ucdavis.edu/classes/mexusenvi/tut11.htm)

22. Shrestha, D. P., Margate, D. E., Anh, H. V. and Van Der Meer, F., Spectral unmixing versus spectral angle mapper for land degradation assessment: a case study in southern Spain. In Proceedings of 17th WCSS, Thailand, Symposium No. 52, Paper 1141, 2002.

23. Varshney, P. K. and Arora, K. M., *Advanced Image Processing Techniques for Remotely Sensed Hyperspectral Data*, Springer-Verlag, Berlin, 2004.

24. Goldberg, D. E., *Genetic Algorithms*, Pearson Education, 2008.

25. Krishna Mohan, B., Classification of remotely sensed images using artificial neural networks. *IETE J. Res.*, 2000, **46**, 401–410.

26. Pangul, R. N., Search algorithms for dimensionality reduction in hyperspectral remote sensing. M Tech dissertation, Indian Institute of Technology, Mumbai, 2014.

27. Tatem, A. J., Lewis, H. G., Atkinson, P. M. and Nixon, M. S., Super-resolution target identification from remotely sensed images using a Hopfield neural network. *IEEE Trans. Geosci. Remote Sensing*, 2001, **39**, 781–796.

28. Gaur, S., Sub-pixel mapping with hyperspectral images using super-resolution, M Tech thesis, Indian Institute of Technology, Mumbai, 2014.

29. Arora, M. K. and Tiwari, K. C., Sub-pixel enhancement in hyperspectral images. *Def. Sci. J.*, 2013, **63**, 63–68.